https://doi.org/10.5194/egusphere-2026-6374
Preprint. Discussion started: 20 November 2026
© Author(s) 2026. CC BY 4.0 License.

A NOAA/GFDL high resolution global ocean/sea-ice configuration for seasonal-to-decadal prediction research: simulation fidelity and marginal ice zone representation

Matthew J. Harrison[1], Theresa Cordero[1], Youngji Joh[1], Robert Hallberg[1], Alistair Adcroft[2], William Cooke[1], Hae-Cheol Kim[3], Colleen McHugh[4], and Utheri Wagura[4]

[1]NOAA/OAR/Geophysical Fluid Dynamics Laboratory, Princeton, NJ, USA
[2]Atmospheric and Oceanic Sciences Program, Princeton University, Princeton, NJ, USA
[3]NOAA/NWS/EMC, Rockville, MD, USA
[4]SAIC

Correspondence: Matthew J. Harrison (matthew.harrison@noaa.gov)

Abstract. A global coupled ocean/sea-ice (MOM6/SIS2) general circulation model configuration at $1/12^\circ$ Mercator resolution (GLBc0p08_OM4) is derived from a $1/4^\circ$ counterpart. As in a prior study, an embedded 3-box model provides a useful freshwater flux constraint in the absence of surface salinity nudging. The horizontal grid and bathymetry are identical to the current NOAA/NWS real-time operational ocean forecast system (RTOFS). This configuration is forced by atmospheric data from the JRA55-do reanalysis (1958-2021), with climatological runoff fluxes from a consistently forced LM4.0 land model simulation. Numerical results are compared to independent observations derived from: in-situ hydrographic profiles, gridded sea-ice and satellite altimetry products, and geostrophic transport estimates from moored instruments and ship-based transects during overlapping time periods.

We highlight the importance of ocean/sea-ice coupling. In the present configuration, the representation of the marginal ice zone (MIZ) is sensitive to the ice/ocean dynamical coupling (CIOD) algorithm; additional subcycle dynamic and sea-ice thickness category distribution updates result in a more realistically compact MIZ, associated with more intense winter sensible heat exchange occurring directly, through changes in sea-ice cover, and indirectly, via meltwater-induced haline feedbacks. In the North Atlantic, robust dense water ventilation occurring near the continental shelves in the Western Labrador and Irminger Seas, south of Svalbard, and in the Barents Seas, are achieved with the subcycling approach; on the other hand, Antarctic coastal ventilation is nearly eliminated through most of the simulation period, due to a lack of wintertime polynya formation. Modifications to the surface energy balance over the Southern Ocean are suggested with this scheme enabled in order to more realistically ventilate the abyssal Southern Ocean.

1 Introduction

Over the past several decades, forecasted trends of Arctic sea-ice decline, increasing upper ocean stratification, and rising global heat content and sea level, due to changes in radiative forcing have emerged from the observational record. Decadal scale projections are subject to initial state and transient response uncertainty, with potentially predictable signals, for instance,

https://doi.org/10.5194/egusphere-2026-6374
Preprint. Discussion started: 20 November 2026
© Author(s) 2026. CC BY 4.0 License.

in the North Atlantic subpolar gyre region (Tulloch and Marshall, 2012; Swingedouw et al., 2013; Biló et al., 2022). Improving ocean and sea-ice model fidelity is vital to our ability to forecast potentially disruptive changes in global weather patterns fueled by air-sea interactions during a period of rapid climate change. The current NOAA/ GFDL hierarchy of fully coupled atmosphere-ocean general circulation models (AOGCM) for seasonal to decadal initialized prediction research use atmospheric and oceanic grids ranging from 1° to 1/4° nominal horizontal resolution (Delworth et al., 2020). We present a new ocean/sea-ice general circulation model (OGCM) configuration, with a 1/12° grid, to be incorporated into the SPEAR (Seamless system for Prediction and EArth system Research) AOGCM suite of experiments, which are derived from the counterpart configuration, CM4 (Held et al., 2019).

By resolving mesoscale deformation scales over a large fraction of the global ocean, eddy-mean-flow interactions are explicitly represented, and upper ocean circulation pathways and properties are expected to become more similar to observations compared to lower resolution models. Model representation of the deep and abyssal circulation is also anticipated to become more realistic with resolution due to improved representation of topography and bottom flow interactions. There are known long-standing OGCM deficiencies in their ability to maintain realistic high latitude dense overflows which have been linked to lack of horizontal resolution, as well as vertical coordinate representation and resolution (Legg et al., 2006).

Arctic and Antarctic overflows supply cold deep and abyssal water to the North Atlantic (2-3°C) and South Pacific, Indian and Atlantic basins (less than 2°C) respectively . In ocean GCMs, spurious mixing and entrainment occur due to three-dimensional advective truncation errors, contributing to poor overflow representation and erosion of deep and abyssal water-mass structure (Winton et al., 1998; Griffies et al., 2000; Ilıcak et al., 2012) The Modular Ocean Model (MOM6) uses an Arbitrary Lagrangian Eulerian (ALE) framework in which vertical truncation errors result from remapping the model state to a dynamically evolving vertical grid. Remapping dispersion errors are largest for Eulerian (geopotential) grids and minimized for Lagrangian (neutral density) targets, although trade-offs exist between these coordinate extremes; e.g. within the surface and bottom layers, fine spatial resolution in weakly stratified regions may be more appropriate. The configuration presented here uses a hybrid coordinate approach, with fixed geopotential interfaces near the surface and portions of the abyssal ocean, and (quasi-Lagrangian) potential density surfaces between (Adcroft, 2019).

Wintertime surface production of dense watermasses drive high latitude overflows and the global thermohaline circulation; e.g., Denmark Strait Overflow Water (DSOW) originates in the Nordic and East Greenland Seas, when cold Arctic air contacts relatively warm ocean temperatures. Surface buoyancy in these regions is strongly controlled by salinity, and deep convection can be effectively shut down during periods of freshwater dominance (Oka et al., 2006; Malmberg and Jónsson, 1997). In the Southern Ocean, high salinity shelf water (HSSW) is formed within coastal polynyas surrounding Antarctica, when katabatic winds displace sea-ice and cool the ocean surface, producing new sea-ice and rejecting brine, resulting in cold and salty watermasses with temperatures near -1.8°C and relatively high salinities near 34.6 PSU (Williams et al., 2008; Kusahara et al., 2010; Portela et al., 2022; Golledge et al., 2025). Downstream entrainment of warmer circumpolar deep water (CDW) results in Antarctic Bottom Water (AABW), which occupies a large fraction of the global abyssal ocean. There exists a strong connection between dense water ventilation on the polar continental shelves and the representation of the MIZ and coastal polynyas.

https://doi.org/10.5194/egusphere-2026-6374
Preprint. Discussion started: 20 November 2026
© Author(s) 2026. CC BY 4.0 License.

In NOAA/GFDL GCMs using the Flexible Modeling System (FMS) coupler, thermodynamic and radiative coupling at the atmospheric lower boundary is calculated implicitly in time on the atmospheric side and within the sea-ice and land models in order to accommodate rapid changes in atmospheric forcing due to clouds, convection and radiation occurring over low heat capacity surfaces. However, due to the lagged dynamic coupling between ocean and sea-ice, GFDL coupled configurations are in some cases formally unstable (Hallberg, 2014). Historically, this has not been a major issue due to dissipative numerics, such as ocean model configurations which strongly damp near-inertial oscillations and/or gravity waves, and/or overly smoothed, viscous representation of sea-ice. Coupling paradigms may need to be re-examined in more energetic and realistic eddying regimes, and with potentially more realistic ice rheology. Accurate predictions of sea-ice, for example in the Barents Seas, is relevant to extended seasonal prediction due to the potential relationship between ice cover in this region and Northern hemisphere weather patterns (Chen et al., 2016; Cohen et al., 2020).

This study documents the configuration of a global eddy resolving ocean/sea-ice model for seasonal to decadal prediction research. Historical simulation results with prescribed atmospheric forcing are compared directly to observations in order to evaluate potential for atmospheric coupling. We discuss model deficiencies and priorities for future development efforts.

2 model configuration and performance

The Ocean Model Intercomparison Project (OMIP-II) (Tsujino et al., 2020) forcing protocol is used to drive the ocean/sea-ice model with 3 hourly JRA55-do reanalysis surface data (1958-2021). We include a freshwater closure estimate as described in a previous study (Harrison et al., 2022) . The implied atmospheric mid-latitude poleward moisture transport is estimated from the historical CMIP6 ensemble and a land model (LM4.0) is consistently forced in order to provide runoff output which takes into account seasonal land storage of liquid and frozen water. In our approach, we avoid the common use of virtual sea surface salinity (SSS) nudging, which renders results more internally consistent (see Appendix A). Ocean surface temperatures are tightly coupled to the reanalysis, via potentially unrealistic sensible and latent feedbacks resulting from the use of specified atmospheric boundary conditions, and cloud and clear-sky radiative feedbacks are additionally not represented in this configuration.

The Sea Ice Simulator (SIS2), with 4 ice layers and a single snow layer, exchanges momentum, mass, salt and enthalpy with the underlying ocean and overlying atmosphere, divided across 5 ice thickness categories, with separate surface area extents for each ice category. SIS2 ice mechanics are treated as a continuum, with internal stresses solved using a viscoplastic rheology solver (Hibler, 1979) with artificial elasticity to render the calculations explicit (Hunke and Dukowicz, 1997; Feltham, 2008). The ice dynamics timestep is 300 seconds. There are 24 sub-cycling steps of the rheology solver per each ice dynamic step and the elastic timescale is equal to 60 seconds. In the present model configuration, SIS2 is parameterized as a more viscous fluid with principal stress components within the plastic yield curve, rather than as a more realistic viscous-plastic media (Kimmritz et al., 2015). As in other similar sea-ice dynamical solvers, SIS2 is prone to dynamic instability due to poorly resolved explicit elastic rheology (Hunke, 2011; Losch and Danilov, 2011). Sea-ice thickness redistribution parameterizations for ridging and landfast ice are not included in the present configuration. Tuning of sea-ice rheology was not undertaken for this study and

https://doi.org/10.5194/egusphere-2026-6374
Preprint. Discussion started: 20 November 2026
© Author(s) 2026. CC BY 4.0 License.

parameter selections were largely based on stability considerations. A partial simulation (not shown) was used to evaluate model sensitivity to additional rheology iterations, which did not appear to significantly impact our results. For simulation results presented here, the iceberg module was disabled, and land frozen discharge is applied to the ocean directly at coastal points rather than as floating ice which melts over time(Martin and Adcroft, 2010).

The ocean model is configured with 75 layers, with a top layer resolution of 2 meters extending to about 50 meters. Interior interfaces are designed to track potential density (σ_2) through much of the interior, although portions of the deep and abyssal ocean, and most of the polar basins, use a fixed geopotential grid. MOM6 uses a split explicit barotropic/baroclinic time-stepping routine in order to separate fast external gravity waves from the slower internal wave field. The barotropic solver uses an adaptive time-stepping algorithm to ensure stability; external and internal mode accelerations are reconciled by the nonlinear continuity solver to preserve positive layer thicknesses (Hallberg and Adcroft, 2009). The baroclinic timestep for momentum and continuity is 300 seconds and the tracer timestep is 1200 seconds. Coriolis terms on the staggered Arakawa C-grid are solved using an enstrophy conserving scheme (Sadourny, 1975) and potential vorticity advection is second order accurate, as in OM4 (Adcroft et al., 2019). Horizontal pressure gradients are calculated using a finite volume approach (Adcroft et al., 2008). Horizontal tracer advection is third order accurate. Vertical ALE remapping is based on third order sub-grid profile reconstructions and target interfaces locations use second order interpolation.

We adopt a simple momentum closure, with dimensional background coefficients, and with resolution scaling based on the grid scale relative to the first baroclinic mode deformation radius (Hallberg, 2013). The harmonic viscosity coefficient is equal to a 0.003 m s^{-1} background velocity multiplied by the grid scale. The biharmonic viscosity coefficient uses a background value of 0.02 m s^{-1}, multiplied by the cube of the grid spacing. For neutral tracer diffusion (Shao et al., 2020), the maximum diffusivity is 500 m^2 s^{-1} and resolution scaling applies. The nominal background vertical diffusion value is 2.0 x 10^{-5} m^2 s^{-1} with a Prandtl number equal to unity (Reichl et al., 2024). Background vertical diffusivities incorporate a latitudinal scaling, as in OM4, based on near-inertial wave-wave interaction eikonal predictions (Henyey et al., 1986; Gregg et al., 2003; Harrison and Hallberg, 2008). Quadratic bottom stress is calculated using the resolved bottom flow, plus a background velocity of 0.001 m s^{-1}. For vertical shear driven mixing, parameter settings are as in OM4 (Jackson et al., 2008). There are no parameterizations for mesoscale eddy mass transport; submesoscale eddies are parameterized following Bodner et al. (2023) and the surface boundary layer scheme follows Reichl and Hallberg (2018).

The ocean/sea-ice grid is identical to the current NOAA/NWS Real Time Ocean Forecast System (RTOFS) with a nominal 8km Mercator projection, a bipolar Northern polar cap, and a grid size of 4500x3528 (Chassignet et al., 2009; Chassignet and Xu, 2021). We present results primarily from a single model simulation (GLBc0p08_OM4_jra_A01, or A01), with 75 vertical levels, there are approximately 1.2 billion grid cells which are distributed in rectangular horizontal domains distributed over 26,370 computational cores on the GAEA HPE-Cray EX3000 NOAA supercomputer. The computational cost is approximately 0.2 million CPU hours per simulation year, or 12.8M CPU hours for the 64 year simulation. MOM6 dynamic and thermodynamic updates account for roughly 44% and 29% of the total ocean cost, respectively, with the remaining costs associated with writing diagnostic output and other auxiliary routines. Overall the ocean accounts for 86%s and the sea-ice about 4% of total runtime (the remaining 10% of runtime are spent within the coupler and performing file I/O for the JRA forcing fields).

https://doi.org/10.5194/egusphere-2026-6374
Preprint. Discussion started: 20 November 2026
© Author(s) 2026. CC BY 4.0 License.

Message passing within the ocean, sea-ice and coupler modules account for roughly 13% of total runtime. SIS2 thermodynamic(dynamic) updates account for about 26%(74%) of the sea-ice cost. Processor domains containing no ocean points are excluded, which reduces computational overhead by approximately 20%.

3 Coupled ice/ocean dynamics

Within the FMS framework, the coupling between component models is separated between a set of "fast" steps for implicit thermal and radiative coupling, and a set of "slow" partially implicit sequential ice/ocean updates for mechanical coupling and mass exchange between these components. In traditional GFDL AOGCMs, fast and slow updates are performed concurrently on separate computational processors, improving job throughput performance at the expense of rendering ice-ocean coupling explicit and potentially more unstable. The slow coupling timestep (Δ_T) between the ocean and sea-ice is susceptible to numerical instability under certain conditions; for example, sea-ice in GFDL simulations does not displace seawater due to difficulty coupling gravity waves and ice rheology on sub-inertial timescales ($\ll \Delta_T$) (Hallberg, 2014). Solving for the joint evolution of sea-ice dynamics and thermodynamics with multiple thickness categories and potentially thin ice is numerically challenging due to the only partially implicit and sequential nature of our coupling approach.

We present novel solutions using a coupled sea-ice/ocean dynamical (CIOD) timestep (Δ_t), with 4 subcycle iterations of ice/ocean dynamics and ice thickness category redistributions ($\Delta_T \Delta_t^{-1} = 4$, see Appendix B for more details); a partial simulation (1958-1974) with traditional sequential coupling ($\Delta_T \Delta_t^{-1} = 1$) is presented for comparison (A02). The sea-ice internal timesteps and the number of rheology iterations are the same in both experiments. Ice-ocean thermodynamic, and mass fluxes are applied once per slow coupled time step ($\Delta_T = 1200$s). The interspersed coupling adds approximately 4% to the overall CPU cost of this configuration. Additional CIOD iterations better reconcile the thermodynamic and dynamic sea-ice states within the partially implicit FMS coupling framework (see Appendix B).

Figure 1 illustrates CIOD sensitivity during late Boreal winter (February-March), 1974; panels (a) and (b) show the ice-lead fraction, defined as the fractional number of days with 20-93% sea-ice coverage within each grid cell; panels (c) and (d) show the maximum monthly average sensible heat flux. Ocean cooling is largest during Winter along the pan-Arctic MIZ, as colder air masses contact the relatively warm open-ocean. Winter heat exchange within the MIZ is suppressed by the presence of fresher surface waters occurring in experiment A02. Using a shorter CIOD time step results in a generally more compact MIZ, while the traditional approach produces a wider MIZ and associated melt zone which fuels surface freshening and stabilization of the mixed layer. Sea-ice congelation freezing and top ice melt rates are not significantly impacted. Observations of MIZ width, for instance south of Fram Strait (Dumont, 2022) vary seasonally from a summer maximum of roughly 100 km, to wintertime values of order 10km. Limited observational comparisons suggests that A02 significantly overestimates the width of the MIZ, while A01 is more realistic.

Similarly, in the Southern Ocean (figure 2), open ocean ventilation at the equatorward sea-ice margins is locally more intense in A01, associated with a more tightly confined MIZ. Ventilation along the coastlines is largely absent in A01 starting in the early 1970's. Figure 3 provides a zoomed in view of the Ross Sea. Despite having a reasonable representation of Antarctic

https://doi.org/10.5194/egusphere-2026-6374
Preprint. Discussion started: 20 November 2026
© Author(s) 2026. CC BY 4.0 License.

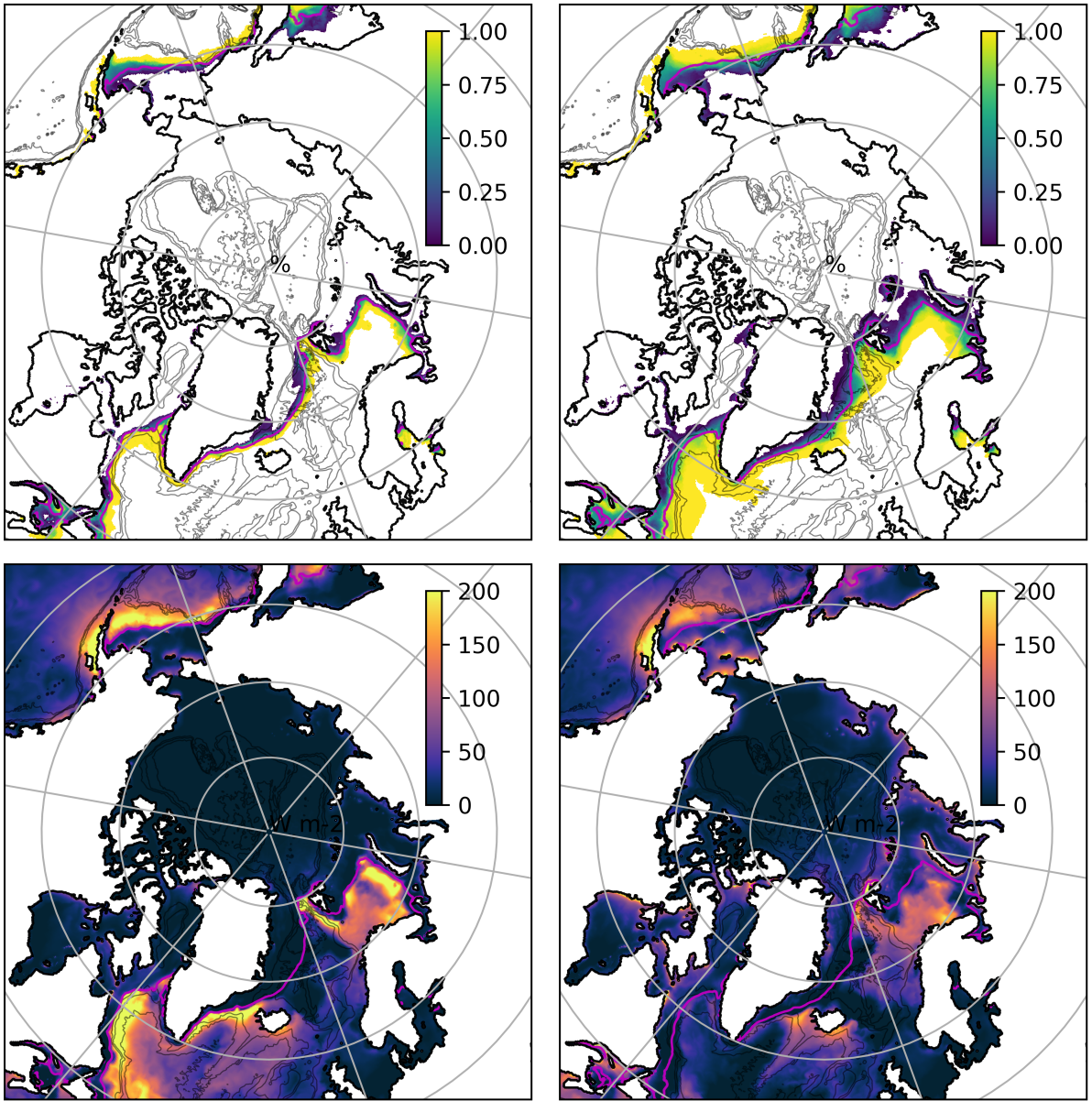


Figure 1. Seasonal ice lead fraction (panels a,b) and sensible heat flux (W m^2, panels c and d) during 1974 Boreal winter. The lefts column (a,c) shows A01 with 4 CIOD iterations, $\Delta_T \Delta_t^{-1} = 4$, and the right columns (b,d) show A02 with without additional CIOD iterations ($\Delta_T = 1200$s in both cases). The time average ice extent is indicated by the magenta contour. A01 has a more confined MIZ in all sectors of the Arctic compared to A02, and this is associated with more intense winter heat exchange and higher SSS (not shown). The ice lead fraction is defined as the fractional number of days with 20-93% sea-ice cover.

https://doi.org/10.5194/egusphere-2026-6374
Preprint. Discussion started: 20 November 2026
© Author(s) 2026. CC BY 4.0 License.

katabatic winds in JRA55-do (Caton Harrison et al., 2022), coastal poylnyas are underrepresented. A longer CIOD timestep in this case allows for coastal ventilation, which is associated with stronger deep and abyssal Southern Ocean ventilation and increased Drake passage transport. Results suggest that reduced sea-ice volume (SIV) in A02 and resulting weaker pack-ice in winter allows for greater lead formation which could otherwise be compensated for by surface energy balance tuning which is beyond the present scope. The lack of Southern Ocean poylnya formation in A01 is perhaps its most consequential bias.

4 Results

4.1 Gulf Stream and Kuroshio Current Systems

Figure 4 compares upper ocean properties between observations from AVISO[1] and OISST (Huang et al., 2021) and the A01 simulation for the 1993–2021 period. The model successfully reproduces the observed subtropical gyre structure and the sharp sea surface height (SSH) gradients associated with both western boundary current extensions (contours in 4a–b). Although EKE is underestimated in the downstream regions of both currents, and EKE near the Gulf Stream separation point along the southeastern U.S. coast is overestimated, the dominant regions of mesoscale eddy activity associated with the western boundary currents are broadly reproduced in the model. Notably, the EKE signature associated with the large-scale stationary meander south of Japan over the Kuroshio Extension and the downstream of Gulf Stream extension path are well captured. Area-averaged monthly SSH anomalies over the Kuroshio Extension (140°E–165E°, 31°N–38°N) and Gulf Stream (75°W–45°W, 31°N–42°N) regions exhibit prominent interannual-to-decadal variability, which is reasonably captured by the model (4c–d).

Point-wise correlations between monthly SSH and SST anomalies reveal strong positive correlations along the western boundary current extensions in both observations and the model (Figures 4e–f), highlighting regions where ocean heat content anomalies are communicated to the surface and subsequently to the atmosphere through turbulent heat fluxes. The realistic SSH–SST coupling captured by A01 reflects the established link between mid-latitude SST fronts and downstream atmospheric circulation, suggesting that integrating this configuration into a coupled framework could enhance seasonal-to-decadal predictability of mid-latitude weather and climate.

4.2 Ocean Heat Content

Observational estimates of historical ocean warming since the mid-20th century range from 200-350 ZJ, or an average rate of 0.4-0.6 Watts per square meter over the ocean (Zanna et al., 2019). Prior to the introduction of the ARGO program, circa 2005 (Riser et al., 2016), which has since provided unprecedented sampling of the upper 2000m, the global oceans were poorly sampled and a large fraction of the data were provided by ships of opportunity (e.g. cargo vessels) networks of expendable bathythermographs (XBT) profiles at depths up to 700 meters (Cheng et al., 2016). Historical deep and abyssal in-situ data are from isolated scientific stations; long term observations suggest that deep and abyssal watermasses are warming more slowly

[1]The altimeter products were produced by Ssalto/Duacs and distributed by Aviso+, with support from Cnes (https://www.aviso.altimetry.fr)

https://doi.org/10.5194/egusphere-2026-6374
Preprint. Discussion started: 20 November 2026
© Author(s) 2026. CC BY 4.0 License.

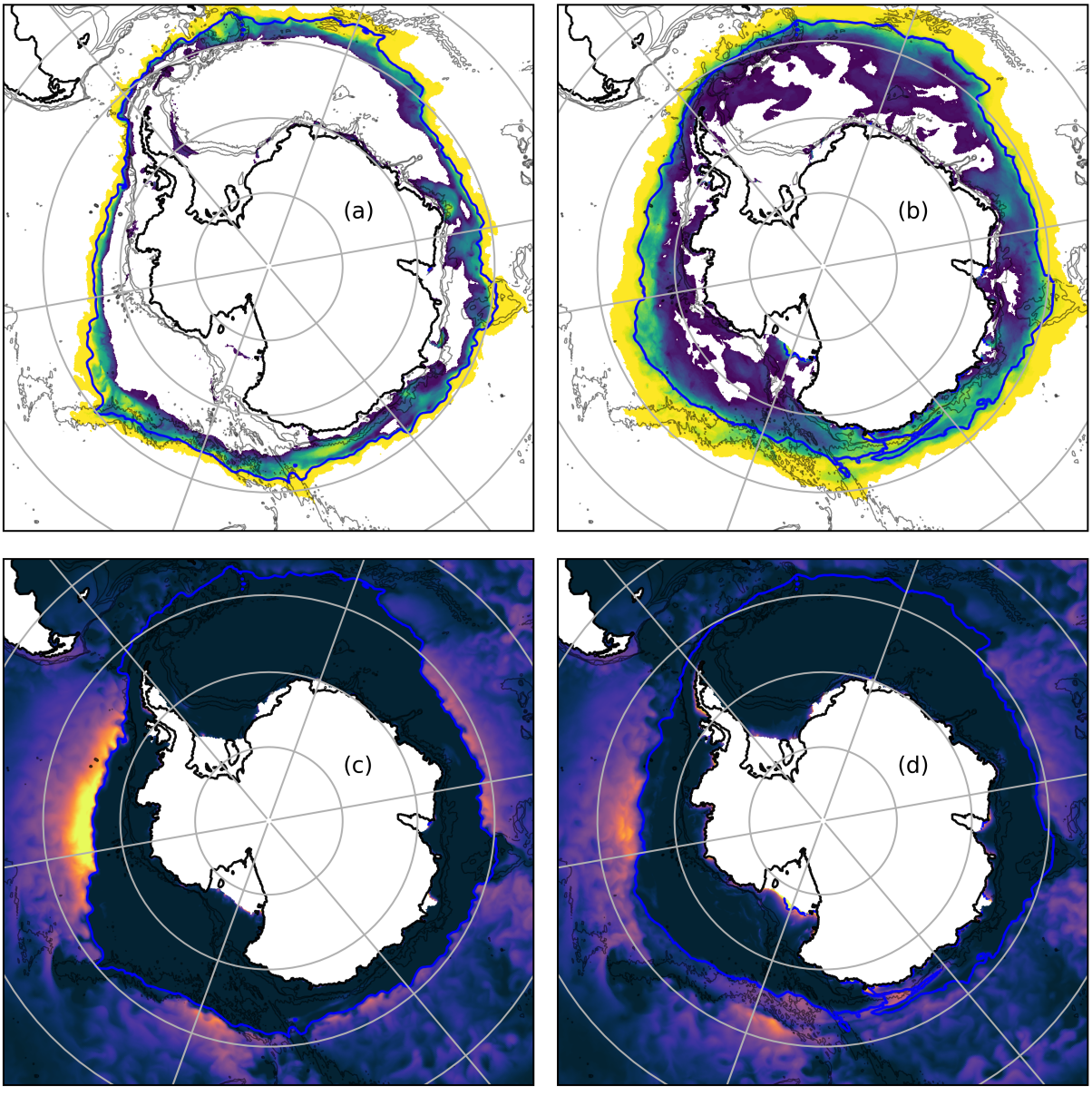


Figure 2. As in figure 1, during August and September, 1974. The Pan-Antarctic sea-ice pack is generally more porous in A02 (right) compared to A01 (left). Sensible heat exchange on the northern pack ice edge is more intense in A01, for instance in the SE Pacific. Thicker ice in A01 is more compact, with negligible lead formation within the winter ice pack.

than above (Johnson and Purkey, 2024). For our observational comparison, we reference the global upper 2km ocean heat

https://doi.org/10.5194/egusphere-2026-6374
Preprint. Discussion started: 20 November 2026
© Author(s) 2026. CC BY 4.0 License.

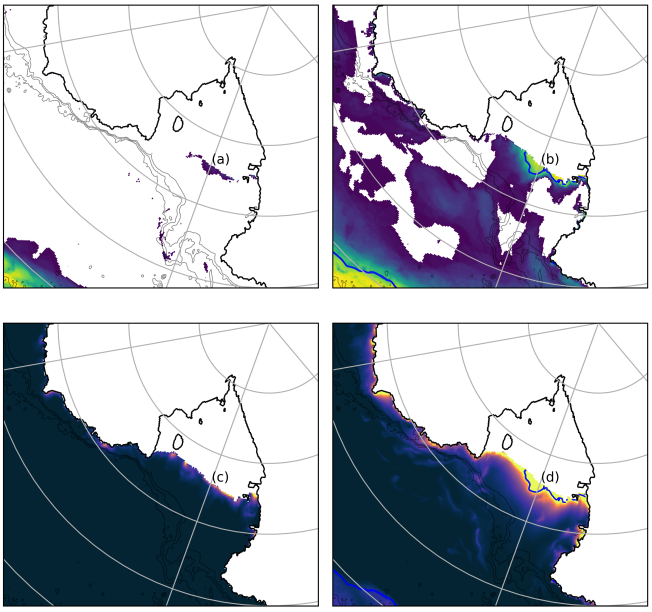


Figure 3. Same as figure 2, localized to the area surrounding the Ross Sea. We highlight that sensible heat exchange is very localized to the coastlines in this simulation and is associated with katabatic wind forcing.

content anomaly (OHCA) dataset from the World Ocean Database (WOD) archived at NOAA/NCEI (Levitus et al., 2012). The model is initialized in 1958 from WOA05 potential temperature and salinity climatology.

Figure 5 shows A01 OHCA accumulated over different depth ranges and compared to WOD. Model cooling in the upper 700-2000m aligns with major volcanic events: Agung (1963), El Chichon (1982), and Pinatubo (1992), consistent with aerosol radiative and cloud response embedded in the JRA55-do surface dataset, although these transient cooling periods are not as readily evident in the WOD analysis. Following Pinatubo, persistent warming in the upper 2km is simulated by the model. Between 1992-2001, A01 accumulates approximately 320 ZJ in the upper 2km of the global ocean, compared to roughly 250 ZJ in WOD. In the deep and abyssal ocean below 2km, simulated heat gain is greater than 200 ZJ, exceeding observational estimates by at least a factor of four (Johnson and Purkey, 2024). The bottom panel in figure 5 shows OHCA in the Southern Ocean (to 34°S). Model deep and abyssal warming originates in the Southern Ocean and accounts for roughly 80% of the global heat content change below 2km in A01. Note that this is reflective of insufficient AABW and coastal polynya formation (section 3).

4.3 Sea-Ice Volume and Extent

Arctic sea-ice is in rapid decline in recent decades, largely at the expense of thick, multi-year ice surrounding the Canadian Archipelago; long term Antarctic sea-ice trends are not evident from the observational record. Passive microwave retrievals

https://doi.org/10.5194/egusphere-2026-6374
Preprint. Discussion started: 20 November 2026
© Author(s) 2026. CC BY 4.0 License.

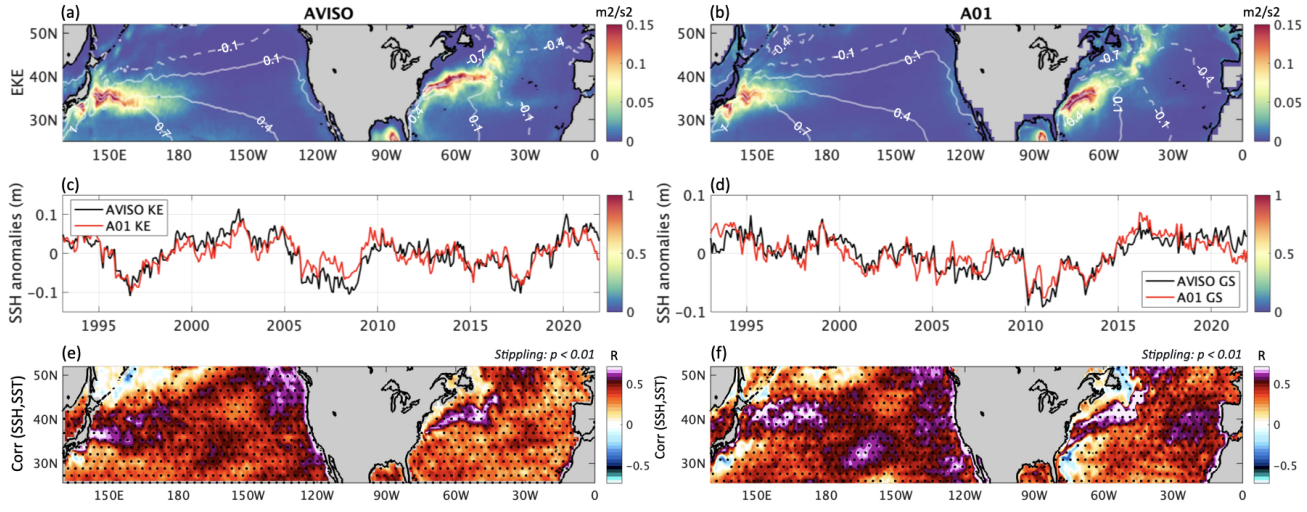


Figure 4. Comparison of observed (left column) and simulated (A01, right column) upper ocean properties over the 1993–2021 period. (a, b) Surface eddy kinetic energy (m^2 s^{-2}) computed from geostrophic velocity anomalies with time-mean sea surface height (m) denoted as contour intervals of 0.1 m (solid) and -0.1 m (dashed). (c) Area-averaged monthly sea surface height anomalies over the Kuroshio Extension region (140°E–165E○, 31°N–38°N) from AVISO (black) and A01 (red). (d) As in (c), but for the Gulf Stream region (75°W–45°W, 31°N–42°N). (e, f) Point-wise correlation between monthly sea surface height anomalies and SST anomalies. Stippling indicates statistical significance at the 99% confidence level.

indicate a decline of roughly 40% in Summer Arctic extent over the past half-century (Cavalieri et al., 1996). Climate model predictions are for a decline towards mostly ice-free Arctic Summers within decades. Ice volume estimates from satellite altimetry are subject to uncertainty due to sampling issues, as well as difficulty accounting for snow on sea-ice (Wang et al., 2022).

Figure 6 shows the northern and southern hemisphere sea-ice volume (SIV) totals in A01 compared to independent estimates from the University of Washington (Zhang and Rothrock, 2003) and altimetry data published by the Copernicus Data Store [2]. The northern hemisphere observational(model) linear trend estimate (1980-2022) is -11%(-12%) per decade; and, the Antarctic SIV observational(model) trend is +14%(+1.3%) per decade. Due to the high volume ratio of northern to southern hemisphere

[2]Copernicus Climate Change Service, Climate Data Store(2020):Sea ice thickness gridded data for the Arctic derived from satellite observations: Copernicus Climate Change Service (C3S) Climate Data Store (CDS) DOI:10.24381/cds6679a99a (Accessed on 07/23/26)

https://doi.org/10.5194/egusphere-2026-6374
Preprint. Discussion started: 20 November 2026
© Author(s) 2026. CC BY 4.0 License.

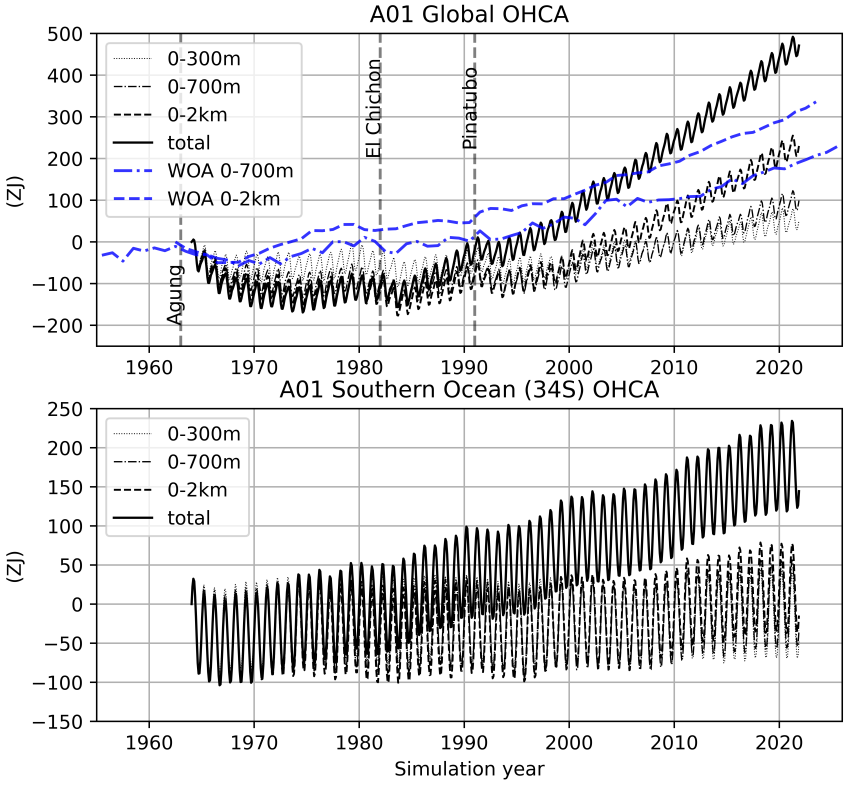


Figure 5. Global heat content anomalies (ZJ): (dotted) 0-300 meters; (dashdot) 0-700m; (dash) 0-2000 meters; (solid) total; (blue dashdot) WOD 0-700m; (blue dash) WOD 0-2km. Bottom panel: As above for the Southern Ocean (90-34°S) (WOD not included). Model OHCA is referenced to the starting value in 1964.

SIV, global trends are dominated by the Arctic. Summer SIV is overestimated in both hemispheres, suggesting a need for model adjustments to the surface energy balance over sea-ice.

Sea-ice extent (SIE) is shown in the Supplemental figures and described here. In the Arctic, ice extent is well represented on decadal timescales in simulation A01, with a nearly identical long term trend in comparison to observations. Simulation A02 is characterized by significantly less Arctic sea-ice in Summer and somewhat more extensive Winter sea-ice relative to A01. Similarly in the Southern hemisphere, A02 produces less extensive Summer ice.

4.4 Ocean Poleward Heat Transport

Quantifying the role of the ocean in the meridional redistribution of heat is fundamental to our understanding of climate. Attempts have been made to constrain the ocean meridional heat transport (MHT) via estimates of top of atmosphere and surface fluxes, and more directly across ocean transects using hydrographic data from ship-based and moored instruments (e.g. Talley (2013); Johns et al. (2023). The top panel in figure 7 shows the global time-average (1980-2021) and annually averaged

https://doi.org/10.5194/egusphere-2026-6374
Preprint. Discussion started: 20 November 2026
© Author(s) 2026. CC BY 4.0 License.

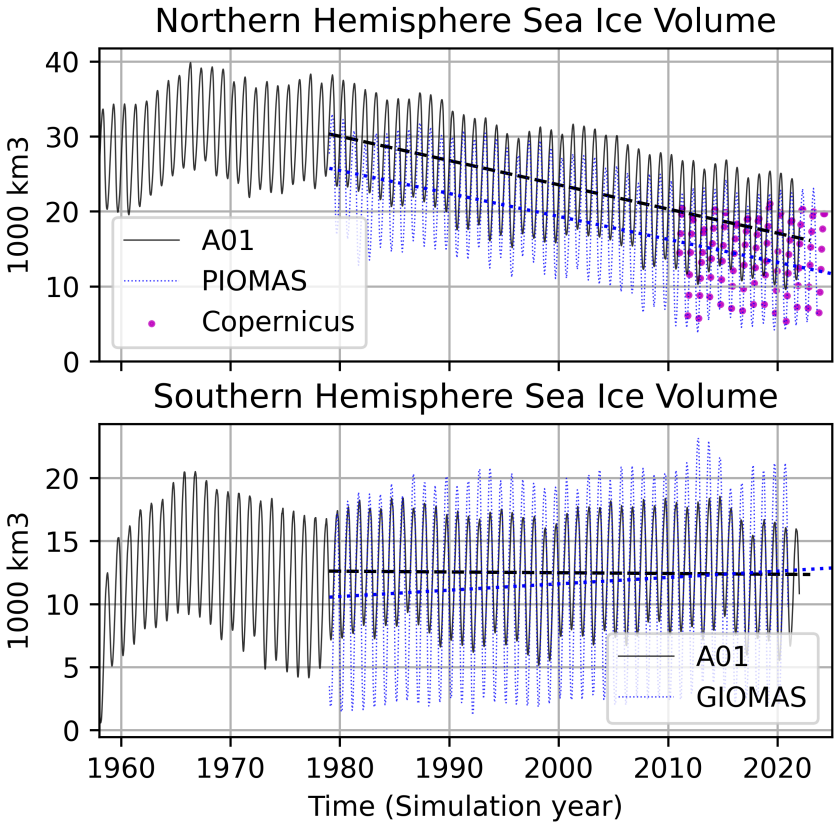


Figure 6. Northern (top) and Southern (bottom) hemisphere sea-ice volume totals for A01 (black) and data assimilative estimates from Zhang and Rothrock (2003) (blue) and Copernicus for the Arctic (magenta). Linear trend estimates for overlapping time period (1979-2021) are indicated by the dashed lines.

MHT in A01, along with an observational estimate (Ganachaud and Wunsch (2003), GW03). The model is within the reported observational range along transects at 30°S, 19°S and 24°N, however, MHT at 47°N is an outlier with the model exceeding GW03 by nearly 25%. The lower panel (figure 7b) shows global (solid) and Atlantic (dashed) MHT at 26°N. A transect-based estimate of 1.3 $\pm$0.14 PW in the Atlantic (2004-2007) exceeds the model average (1.17 PW) for the overlapping time period. The global 26°N transport is fairly steady throughout the simulation period, at approximately 1.8 PW, while the Atlantic contribution at this latitude peaks in 1994 at nearly 1.4PW, has a minimum value in 2010 of roughly 0.7PW, and is declining at an annual rate of 0.2% over the past four decades.

4.5 Indonesian Throughflow (ITF)

ITF variability can be generally understood as a response to wind forcing using the island rule (Godfrey, 1996), pluss a contribution from the thermohaline circulation, involving upwelling of denser waters from below the depths of the Indonesian

https://doi.org/10.5194/egusphere-2026-6374
Preprint. Discussion started: 20 November 2026
© Author(s) 2026. CC BY 4.0 License.

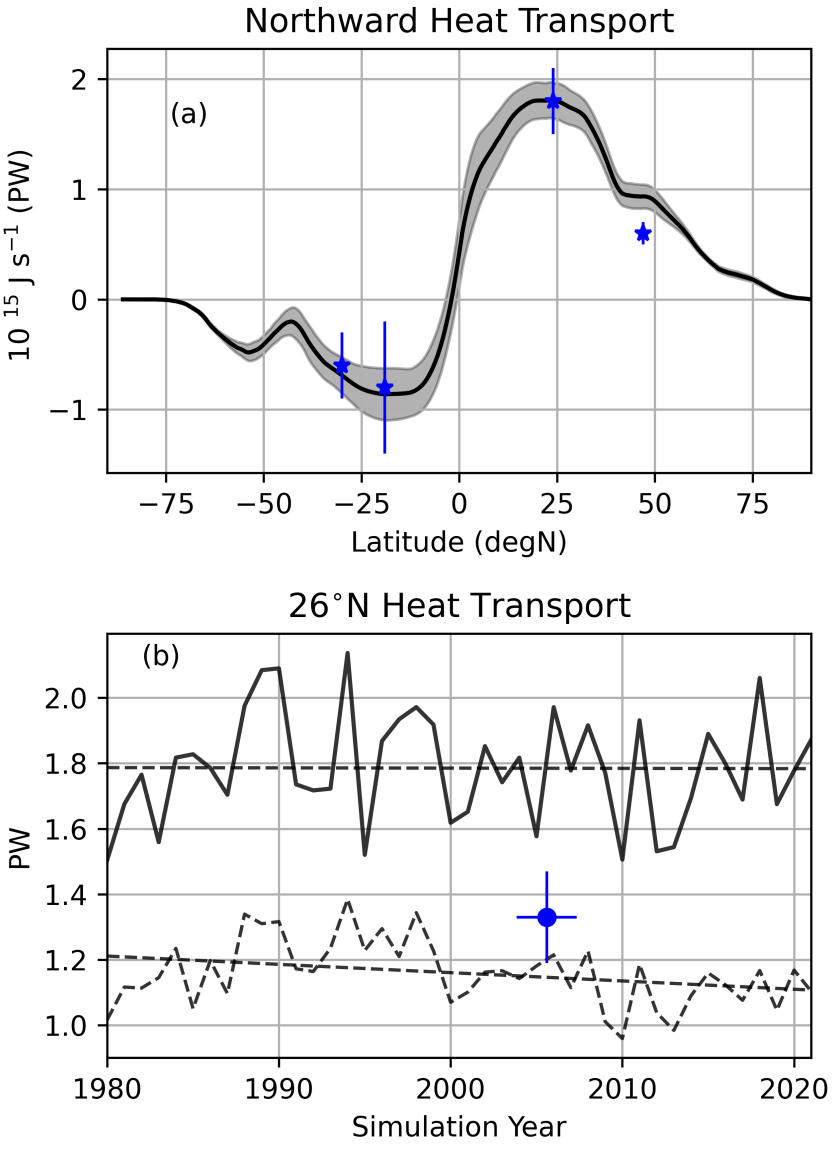


Figure 7. (a) Time mean A01 (1980-2021) global MHT (black line) and interannual range (shaded) as a function of latitude, with observational estimates (Ganachaud and Wunsch, 2003) in blue; (b) MHT at 26°N: total (solid) and Atlantic (dashed) with corresponding linear estimates and the Johns et al. (2011) estimate in blue.

passages. Model thermohaline drift is anticipated due to basin-wide advective-diffusive imbalances resulting from highly parameterized diapycnal mixing.

A01 is consistent with observed flow through Makassar Strait which is primarily southward; Lifamatola Strait flow reverses with depth, with dense southward overflows entering the Banda Sea below 600 meters and warmer surface water flowing

https://doi.org/10.5194/egusphere-2026-6374
Preprint. Discussion started: 20 November 2026
© Author(s) 2026. CC BY 4.0 License.

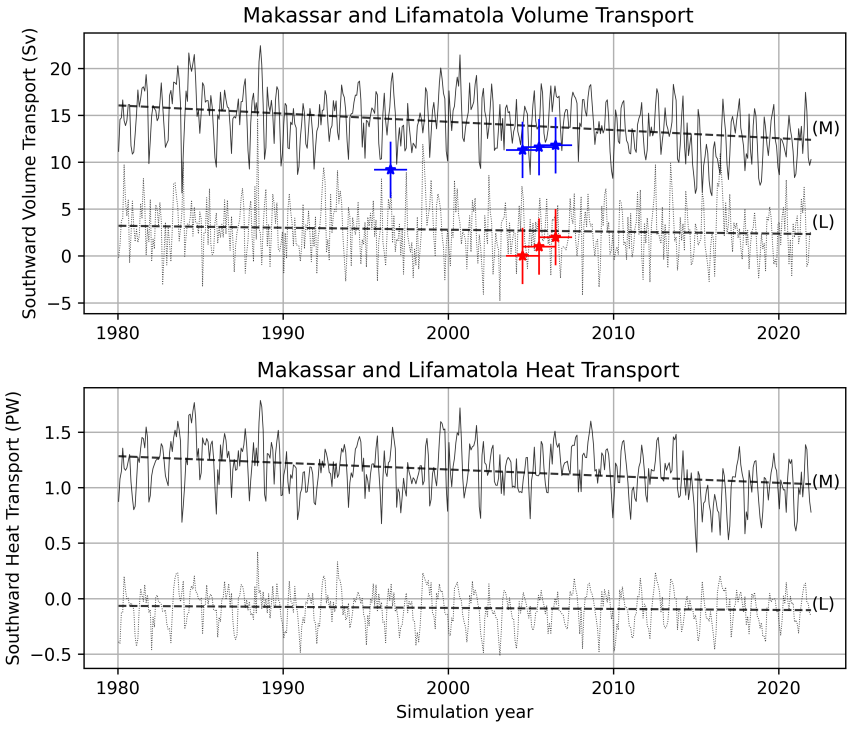


Figure 8. Flow through the Makassar and Lifamatola passages; the top panel (a) shows A01 net southward flow through Makassar Strait (black), and Lifamatola (grey) in units of 10^6 m^3s^{-1} (Sv) along with INSTANT observations for Makassar (blue) and Lifamatola (red). Observational results are annual mean values and the vertical bars correspond to a standard deviation estimate reported by the authors. Model linear trend estimates are indicated by dashed lines. The lower panel (b) shows A01 net southward transport of heat in units of 10^{15}J s^{-1} (PW) for Makassar (black) and Lifamatola (grey). Note that the model heat transport through Lifamatola passage is southward on average, indicative of strong vertical exchange between the Sulawesi and Banda Seas (van Aken et al., 2009)

northward into the Pacific (van Aken et al., 2009). The exit points of the ITF are along the Sunda Archipelago: Timor, Ombai and Lombock Straits. Figure 8 shows the model mass and heat transports through Makassar and Lifamatola Straits, along with results from a recent observational campaign.

The International Nusantara Stratification and Transport (INSTANT) Program deployed moored instruments from 2004-
240 2006 in the ITF passages (Gordon et al., 2010): time-mean observed(model) transports at Makassar and Lifamatola are 11.6(14.2)Sv, and 1.0(2.8)Sv, respectively during the observation period. Longer term model trends in both channels are for weakening ITF transport between 6-7% per decade. While climate models suggest that in warming climate scenarios the ITF transport will weaken in response to slowdown in the global thermohaline circulation, longer term ITF trends in this simulation may be the result of basin-scale advective-diffusive imbalance in the Pacific and not necessarily the consequence of a
245 thermohaline circulation reduction in response to atmospheric forcing changes.

https://doi.org/10.5194/egusphere-2026-6374
Preprint. Discussion started: 20 November 2026
© Author(s) 2026. CC BY 4.0 License.

4.6 Drake Passage

Surface buoyancy transformation and winds in the Southern Ocean plays a pivotal role in the establishment of the global pycnocline (Gnanadesikan and Hallberg, 2000); these forces, in combination with ocean eddy fluxes determine the stratification of the ACC and its volume transport through Drake Passage (Meredith et al., 2011). The response of the Southern Ocean circulation to changes in windstress associated with, for example, the Southern Annular mode (SAM) are understood in terms of the role of eddies on the residual meridional overturning circulation on annual and longer timescales (Hallberg and Gnanadesikan, 2006).

The International Southern Ocean Studies (ISOS) measured the yearlong 1980 transport across Drake passage at approximately 134 Sv with a standard deviation of approximately 11 Sv. Longer term transect based estimates are roughly between 125-150 Sv (Meredith et al., 2011). The average model transport through Drake passage for the 1980-2021 simulation period is 104 Sv with a linear trend estimate of -1.2 Sv per decade (figure 9). Weak Antarctic coastal ventilation in A01 appears to be a major contributor to the model ACC bias. A02 was shown to ventilate the Southern Ocean through coastal polynyas in section 3 (using a longer CIOD timestep). The 1964-1974 average Drake passage transport(normalized trend) in A02 is 134 Sv(-10% per decade), whereas A01 is equal to 105 Sv(-20% per decade) for the same time period (not shown).

4.7 North Atlantic: RAPID-MOCHA and OSNAP

The RAPID-MOCHA-WBTS array at 26°N in the Atlantic provides a unique dataset for model evaluation[3] (Johns et al., 2023; Moat et al., 2026). At this latitude, transport is divided between the Florida channel and the open basin to the East. Bottom pressure moorings placed across the continental slope provide a geostrophic estimate of the depth-integrated transport between mooring depths. Climate models are typically inadequate at representing the deep circulation due to deficiencies related to dense water production, overflow representation and parameterized diapycnal mixing in general. Simulation A01 shows considerable agreement with observations of the upper and deep components of AMOC at the RAPID-MOCHA array.

In figure 10, we show the observed(model) AMOC index, defined as the maximum cumulative basin northward transport in depth space starting from the surface. The 2005-2021 average value is 17.0(18.1)Sv. The deep AMOC index, defined as the maximum cumulative basin southward transport starting at 3000m below the surface, is 5.8(7.1) Sv. The model exhibits impressive agreement with independent geostrophic transport estimates across timescales, with similar decadal trends. The observational(model) 2004-2021 linear trend of the northward AMOC index is -0.87(-0.67) Sv per decade. The deep circulation trend is -0.79(-0.34) Sv per decade. For the deep circulation index shown in figure 10b, we note that the model reproduces the sharp reduction in transport from roughly 10 Sv in 2005 to a minimum value near 0 Sv in 2010. This was followed by a gradual recovery through 2018, after which there is less agreement, as simulated AMOC deep export appears to be developing a positive bias.

Hydrographic transects at the OSNAP array (figure 11) illustrate the connectivity between the Atlantic and Arctic basins; Northward inflow of warm/salty Atlantic water along the eastern boundary (near Rockall Trough to the right) is balanced by out-

[3]The RAPID-MOC monitoring program is funded by the Natural Environment Research Council and data is freely available from www.rapid.ac.uk

https://doi.org/10.5194/egusphere-2026-6374
Preprint. Discussion started: 20 November 2026
© Author(s) 2026. CC BY 4.0 License.

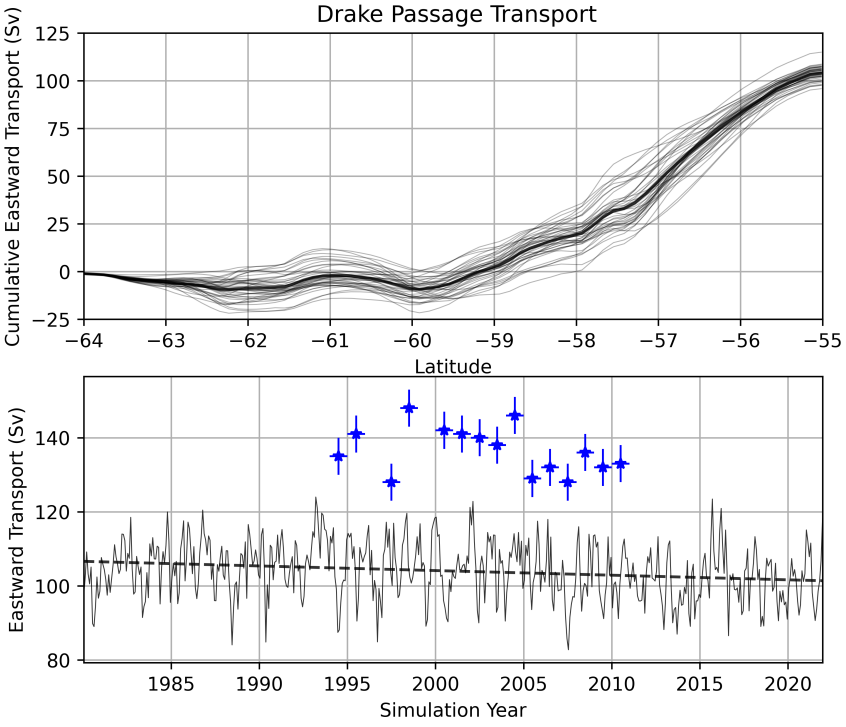


Figure 9. Top panel: the cumulative eastward transport (Sv) at Drake Passage as a function of latitude plotted for individual years (1980-2021), the time mean transport is shown by the thick black line; Bottom panel: Total Drake Passage eastward transport (Sv) timeseries. Observational estimates from UK repeat hydrology cruises (1993-2009) are indicated by the blue dots with the standard deviation estimate indicated by the vertical bars.

flows of relatively cold and fresh waters of Arctic origin east of Reykjanes Ridge, off East Greenland and on the western side of the Labrador basin. Upward tilting isotherms along the eastern ridge flanks in observations are indicative of bottom-intensified Southward outflows, which are only partly represented by the model. In the upper ocean, the Atlantic inflow through Rockall trough is too salty, and mid-depth stratification in the Irminger and Labrador Seas is too weak. Near bottom temperatures are biased warm across the transect. Interior hydrographic biases appear to be largely independent of horizontal resolution (based on comparisons to lower resolution simulations not shown here). Known deficiencies in the internal mixing parameterizations in this configuration, in addition to the sub-optimal vertical grid representation appear account for persistent Arctic overflow biases. For additional discussion of Arctic overflows observations and modeling challenges, see e.g., New and Smythe-Wright (2001); Østerhus et al. (2008); Käse et al. (2003); Legg et al. (2006).

https://doi.org/10.5194/egusphere-2026-6374
Preprint. Discussion started: 20 November 2026
© Author(s) 2026. CC BY 4.0 License.

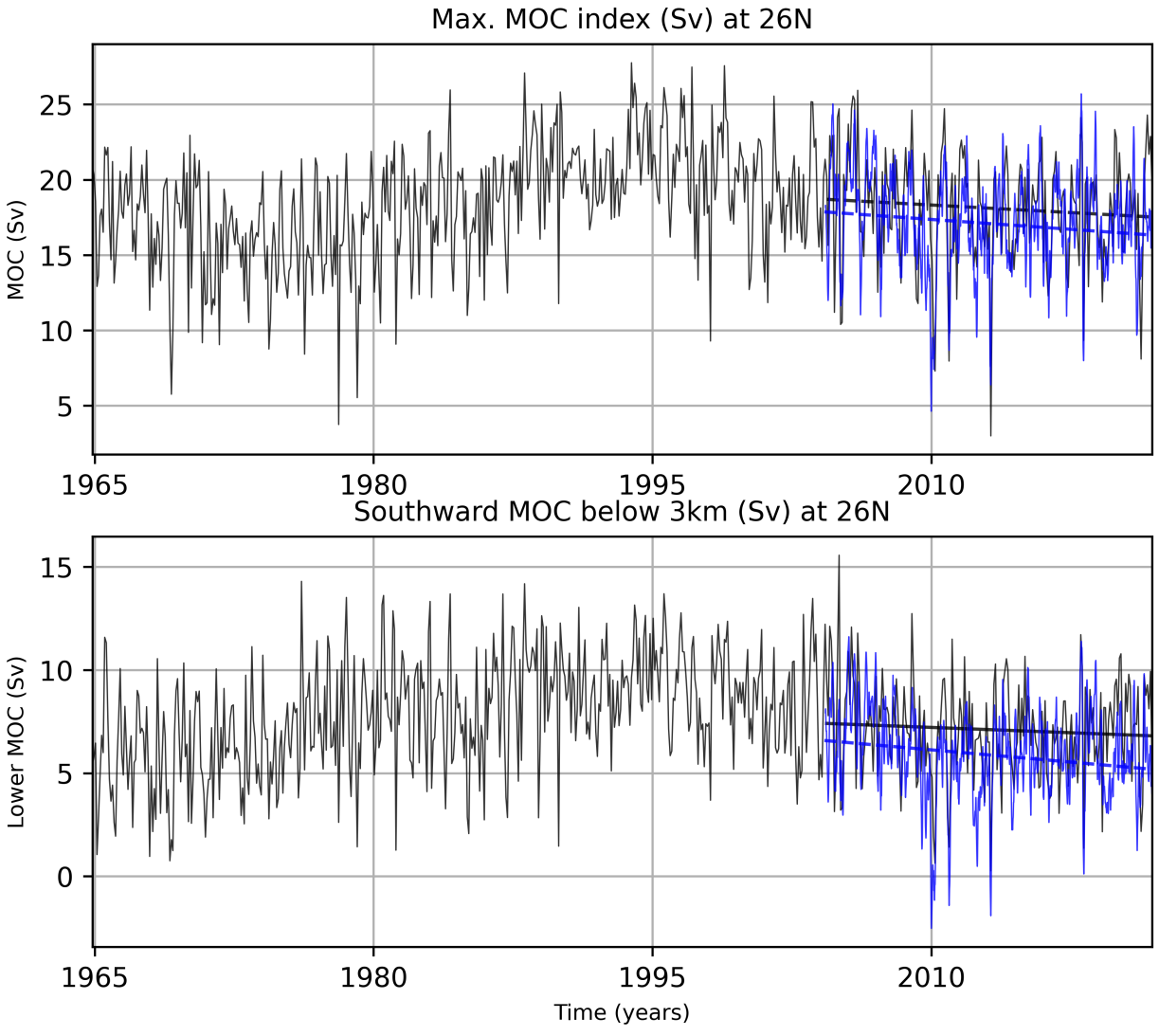


Figure 10. Observational estimates (blue) and model simulation (black) at the RAPID-MOCHA array at 26°N. The top panel (a) shows the MOC index (Sv), defined as the maximumum zonally integrated northward transport, integrated downward from the surface. The bottom panel (b) shows the deep AMOC index, defined as the peak in the zonally and vertically integrated southward transport occurring below approximately 3000m depth. Model transports are monthly averages and the 12 hourly RAPID-MOCHA data are smoothed with a 30 day boxcar filter.

5 Summary

This study documents an atmospheric reanalysis forced simulation, using a global $1/12^{\circ}$ MOM6/SIS2 OGCM configuration (GLBc0p08_OM4) which has been incorporated into the NOAA/GFDL SPEAR AOGCM ensemble hierarchy for seasonal to

https://doi.org/10.5194/egusphere-2026-6374
Preprint. Discussion started: 20 November 2026
© Author(s) 2026. CC BY 4.0 License.

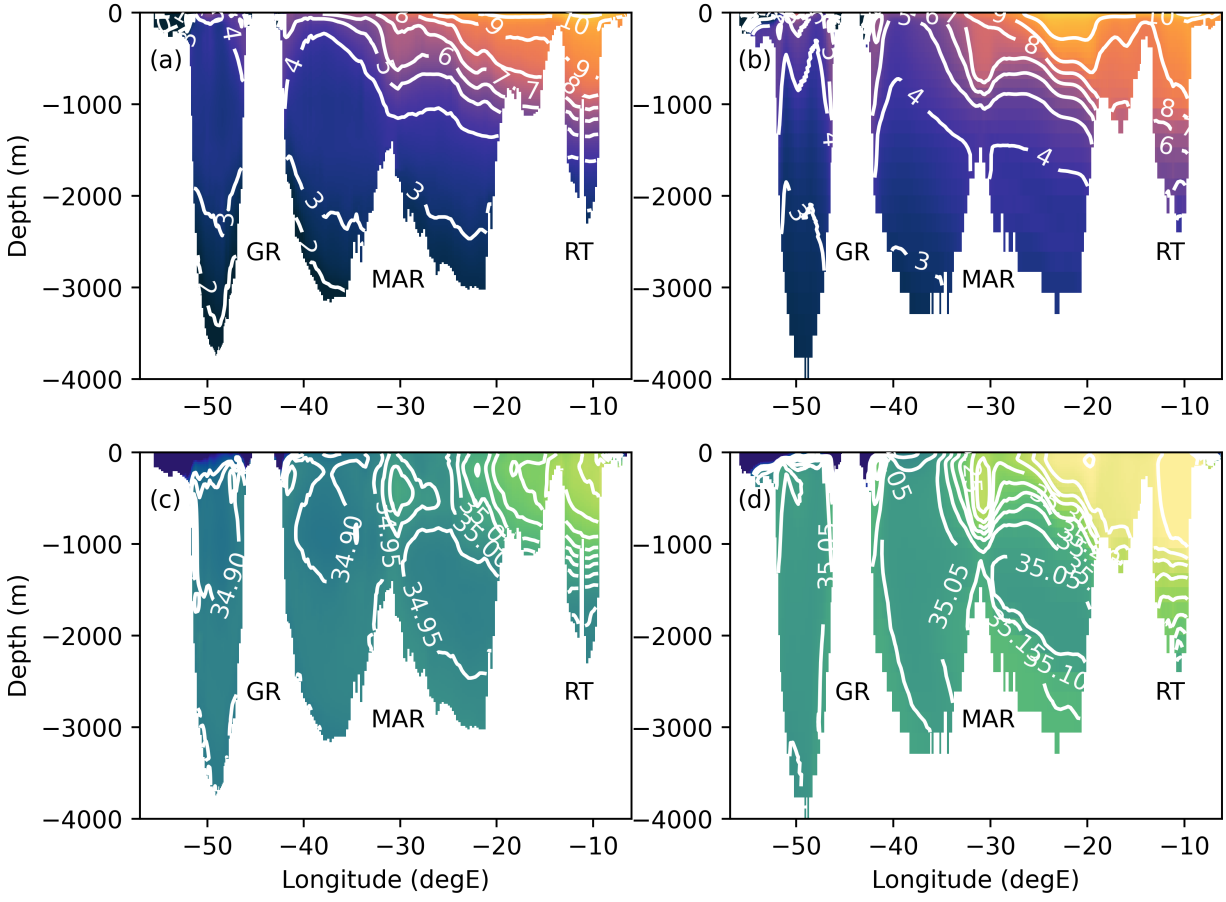


Figure 11. OSNAP transect climatology (2014-2018) (a) potential temperature and (c) practical salinity; Arctic overflows are indicated by the near bottom layer of cold water which tilts into the bathymetry along the mid-Atlantic ridge and east of Greenland. Model potential temperature (b) and salinity (d) climatology during the OSNAP observational period. Note the relatively warmer model bottom temperatures and watermass biases in the Irminger and Labrador Seas.

decadal prediction research. Additionally, we introduce a modification to the ocean/sea-ice coupling in the FMScoupler as part of ongoing model development and planned implementation in SPEAR.

While the mean positions of the Gulf Stream and Kuroshio boundary currents are well represented by the model, the downstream regions have a weak eddy kinetic energy bias which should receive further attention in subsequent studies. Results suggest that this model configuration will provide credible ocean dynamical representation for western boundary current regions, particularly in the Pacific, which may impact seasonal to decadal forecast performance.

Global ocean heat content anomalies above 2km are fairly consistent with observations; however, the deep Southern Ocean warms unrealistically below 2km after 1983, presumably due to a lack of AABW production, resulting from an underestimation

https://doi.org/10.5194/egusphere-2026-6374
Preprint. Discussion started: 20 November 2026
© Author(s) 2026. CC BY 4.0 License.

of coastal poylnya formation in this simulation. Episodic late 20th century upper 2km global cooling following major volcanic events is a feature of these simulations which is difficult to constrain observationally due to the relatively limited observational network prior to the introduction of the ARGO global ocean monitoring program in 2005.

Sea-ice is an important indicator of the climate state, and while the lack of atmospheric feedbacks is a clear limitation of these simulations, our results provide an observationally consistent representation of Arctic sea-ice decline over the past 40 years. Positive Summer sea-ice extent biases exist in both hemispheres (see supplemental figure). Improved representation of sea-ice rheology and physics should be considered in future model development efforts (Hunke et al., 2017); for example, sea-ice melt ponds, land-fast ice, and mechanical ridging are not accounted for in the present configuration.

Transports through the major Indonesian passages are in fair agreement with limited observational estimates, however potential biases may exist due to, for example, basin scale wind biases and/or advective-diffusive imbalances from highly parameterized diapycnal mixing. Drake passage transport is significantly under estimated, and we provide evidence that this bias is connected to poor model representation of Antarctic coastal polynyas.

The deep and abyssal circulation in the Atlantic basin is monitored closely at the RAPID-MOC array at 26°N since 2004; model representation of the northward upper ocean circulation and southward deep and abyssal branch indicate remarkable agreement with independent estimates; however, simulated Atlantic poleward heat transport may be underestimated. We have not accounted for changes in Arctic and Antarctic freshwater budgets due to glacial mass loss, nor have we considered changes in the atmospheric moisture transport, both of which are expected to increase in response to emergent global warming. We speculate that model overestimation of lower North Atlantic Deep water export in recent years (figure 10, panel b) may be related to missing Arctic freshwater sources in this simulation. Despite strong agreement with observations for the lower limb of AMOC, the model exhibits poor Arctic overflow representation, likely due to known inadequacies in the vertical coordinate representation in OM4 (Adcroft et al., 2019) .

We highlight MIZ sensitivity to additional iterations of ice-ocean dynamics and thickness distributions adopted for this study. While inertial ice-ocean coupling is well resolved with the traditional approach, additional CIOD iterations improve the reconciliation of ice thickness categories, particularly near the rapidly evolving pack ice edge, preventing thinner ice from extending the MIZ globally. Dense water production is strongly impacted, particularly in regions with warm water inflow towards pack ice, such as in the northern GIN Seas (see figure 1). Additional CIOD iterations result in a more confined MIZ along the equatorward flanks of the pack ice in both hemispheres, with associated stronger wintertime surface buoyancy loss and, for example, a significantly deeper AMOC circulation. Alternatively, coastal wintertime ventilation along the Antarctic coast was suppressed by additional CIOD iterations due to losses in coastal polynya area, which in turn led to unrealistic deep and abyssal heat uptake and under-estimated Drake passage transport. We recommend the adoption of the CIOD approach for future GFDL-based configurations, although re-tuning of the sea-ice surface energy balance needs to be considered in order to reduce sea-ice biases and improve the ventilation of the abyssal Southern Ocean. Furthermore, for OGCM studies, we emphasize the importance of consistency in the treatment of the global water cycle (see Appendix A). The model simulation demonstrated in this study does not incorporate artificial SSS feedbacks or damping towards a prior, rendering results more internally consistent with regard to haline feedbacks, thus providing further confidence in model results.

https://doi.org/10.5194/egusphere-2026-6374
Preprint. Discussion started: 20 November 2026
© Author(s) 2026. CC BY 4.0 License.

Code availability. The exact source code used for GLBc0p08_OM4 is archived on Zenodo (Harrison, 2026a)

Data availability. MOM6/SIS2 input parameter files are archived on Zenodo(Harrison, 2026a). JRA55-do forcing data are downloadable from the ESGF network (Tsujino, 2018). A subset of model results are available from Zenodo (Harrison, 2026b). Additional files needed to reproduce results from this manuscript are available upon request.

Appendix A: Appendix A: surface mass balance closure

Historically, very little attention has been paid to the representation of freshwater fluxes in ocean models (Roullet and Madec, 2000). A common approach assumes limited knowledge of the surface mass flux and in compensation introduces a nudging to a climatological sea surface salinity (SSS), thereby introducing unphysical feedbacks between SSS and freshwater fluxes due to strong correlations between these fields. Additionally, the globally integrated surface mass flux over the ocean must vanish on interannual and longer timescales, assuming there are no sources or sinks occurring over land.

In Boussinesq (volume conserving) or non-Boussinesq (mass conserving) explicit free surface ocean models with natural boundary conditions for freshwater,

$$\partial_t(\rho\eta) = \nabla\cdot(\rho U) + P - E + R, \tag{A1}$$

where η is the height of the sea surface (accounting for the presence of sea-ice) with representative density ρ, $\nabla\cdot\rho\bar{U}$ is the depth integrated horizontal mass flux divergence (including sea-ice) forced by atmospheric precipitation (P), evaporation(E) and land runoff fluxes (R). Global Boussinesq volume (or non-Boussinesq mass) balance is achieved in fully coupled AOGCMs due to flux conservative models (i.e. globally vanishing first rhs term in A1) and flux exchange between components, however ad-hoc procedures are required for OGCMs with sea-ice coupling.

In one approach, a rescaled precipitation ($P^* = \alpha P$) and runoff ($R^* = \alpha R$), is substituted in equation (A1) (e.g. Adcroft et al. (2019)) using a single parameter, α such that the total adjusted surface mass balance (SMB) over the ocean domain (Ω_o) with coastlines (Σ) vanishes,

$$F_{\Omega_o} = \iint (P^* - E)d\Omega_o + \int R^* d\Sigma = 0. \tag{A2}$$

While this adjustment effectively prevents global ocean mass drift, it introduces avoidable errors. Alternatively, consider the combined land and ocean boundary Ω, wherein the globally integrated atmospheric flux,

$$F^*_{\Omega} = \iint (P^* - E)d\Omega, \tag{A3}$$

https://doi.org/10.5194/egusphere-2026-6374
Preprint. Discussion started: 20 November 2026
© Author(s) 2026. CC BY 4.0 License.

is assumed to vanish (ignoring actual moisture residence times from days to weeks). This approach allows for seasonal land storage and release. Climatological runoff fluxes are provided from a similar model configuration which includes the land model. Two additional degrees of freedom are supplied by a 3-box model for freshwater; SMB is constrained for northern ($\varphi > \varphi_n$) and southern ($\varphi < \varphi_s$) domains based on climatological transport estimates from AOGCM historical simulations, i.e. for the northern sub-domain:

$$F^*(\varphi > \varphi_n, t) = \langle F_n^i(\varphi > \varphi_n, t = t_c) \rangle, \tag{A4}$$

where $\langle F(t = t_c) \rangle$ represents an ensemble climatological average of CMIP6 historical fluxes (F^i). Advantages of the SMB approach relative to traditional methods are: (1) realistic global mass closure accounting for seasonal land storage; (2) the elimination of unrealistic SSS-SMB feedbacks; and, (3) the incorporation of climatological atmospheric meridional moisture transport constraints based on fully coupled AOGCMs. For the present study, $\varphi_{n/s} = 40°$N/S and SMB adjustments are appied at the atmospheric boundary (not at the ice-ocean interface), thus ensuring a consistent representation of internal mass exchange between ocean and sea-ice (Harrison et al., 2022).

Appendix B: Appendix B: ice-ocean coupling

It is fairly standard practice in modern AOGCMs to represent sea-ice using an underlying grid cell thickness distribution, with corresponding areas, for the purposes of thermodynamic coupling with the atmosphere and ocean. The joint solving of enthalpy and thickness distribution in a conservative AOGCM context presents numerical challenges which have been addressed in previous studies (Winton, 2000; Zhang and Rothrock, 2001, 2003). For sea-ice advection, the ice is treated as continuum, i.e. with combined ice thickness categories. Between ice dynamic steps, iterations of a rheology solver are applied in order to represent deformation due to EVP internal stresses. EVP rhelogy is not discussed here, but the presence of rheology raises additional numerical issues regarding the reconciliation of rapidly evolving sea-ice due to both external and internal forces, with potentially thin sea-ice.

Following Hallberg (2014), we use a toy example to demonstrate CIOD coupling between the ocean and sea-ice, with respective boundary layer density (ρ), thicknesses (h), temperature (θ) and velocity (u) using serial execution between the sea-ice and ocean. Within each grid cell, the ice-ocean heat exchange is divided between ice thickness categories defined by the area distribution function (Γ, Thorndike et al. (1975)),

$$Q_{io}(T) = \int K(\theta_o(T) - \theta_i^*(T+1)) d\Gamma, \tag{B1}$$

based on ice-ocean thermal contrast using a piston velocity, K. The heat flux computation is necessarily made implicit due the existence of thin ice categories, and the asterisk indicates that the sea-ice state is only partially updated for thermodynamic fluxes and does not include lateral updates. Sea-ice enthalpy ($\Theta = \rho_i c_p h_i \theta_i$) updates apply the previously computed top (Q_{ia}), and bottom of ice fluxes over the coupling timestep (Δ_T),

https://doi.org/10.5194/egusphere-2026-6374
Preprint. Discussion started: 20 November 2026
© Author(s) 2026. CC BY 4.0 License.

$$\Delta_T^{-1}(\Theta_i^*(T+1) - \Theta_i(T)) = Q_{ia}(T) + Q_{io}(T). \tag{B2}$$

Mechanical coupling is represented by a constant coefficient (γ). Ice velocities (u_i) are only partially implicit due to the use of intermediate ice thickness (h_i^*),

$$\Delta_T^{-1}(u_i(T+1) - u_i(T)) = -\frac{\gamma}{\rho_i h_i^*}(u_i(T+1) - u_o(T)). \tag{B3}$$

Ice dynamic updates are followed by ocean dynamics,

$$\Delta_T^{-1}(u_o(T+1) - u_o(T)) = -\frac{\gamma}{\rho_o h_o(T)}(u_o(T) - u_i(T+1)) \tag{B4}$$

The final ice update involve advection of ice thickness distribution and lateral processes including ridging and rafting (Ψ),

$$\Delta_T^{-1}(\Gamma(T+1) - \Gamma^*) = -U_i \cdot \nabla\Gamma^* + \Psi, \tag{B5}$$

This is followed by explicit thermodynamic ocean updates using previously computed fluxes from the atmosphere over ice-free regions (Q_{oa}) and under sea-ice, in flux form,

$$\Delta_T^{-1}(\Theta_o(T+1) - \Theta_o(T)) = Q_{oa} - Q_{io} + Q_{ml} - \nabla \cdot (U_o\Theta_o), \tag{B6}$$

where Q_{ml} is the advective/diffusive heat flux at the base of the mixed layer, and $\nabla \cdot (U_o\Theta_o)$ is the lateral advective divergence.

In most GFDL fully coupled AOGCM configurations, the sea-ice state in equations (B3, B4, and B5) is concurrent with the ocean, which renders dynamic coupling explicit and formally unstable. The potentially unstable nature of ice-ocean coupling, has motivated software development in the FMScoupler[4] in order to better represent coupled interactions, with the eventual goal of fully embedding the sea-ice and ocean models as a single component in order to facilitate fully implicit flux calculations, and to allow for a more complete representation of ice/ocean dynamic interactions, e.g. between ocean surface gravity waves and rapidly evolving internal ice dynamics. The CIOD implementation demonstrated in this study allows for additional iterations with a reduced timestep, Δ_t, in equations (B3, B4 and B5), between thermodynamic coupling timesteps (eqns. B1 and B2). Additional CIOD iterations dramatically impact simulation results, suggesting that additional reconcilation of the dynamically evolving ice thickness distribution, as well as more tightly integrated ice-ocean dynamic interactions improve observational fidelity of model simulations.

[4]https://github.com/NOAA-GFDL/FMScoupler/tree/main

https://doi.org/10.5194/egusphere-2026-6374
Preprint. Discussion started: 20 November 2026
© Author(s) 2026. CC BY 4.0 License.

Results without additional CIOD iterations ($\Delta_T \Delta_t^{-1} = 1$) appear converged for coupled timesteps (Δ_T) less than 1 hour (figure S1), indicating that ocean-ice dynamic interactions are well resolved. However, we encountered a sensitivity to the number of CIOD iterations, despite having no indication of ice-ocean dynamic coupling instability. This is illustrated by comparing two simulations which are identically initialized with (A) $\Delta_T \Delta_t^{-1} = 1$, and (B) $\Delta_T \Delta_t^{-1} = 4$, with $\Delta_T = 1200$s in both cases. Figure S2 shows the ice lead fraction and bottom melt heat fluxes during Winter. In general, the more extensive MIZ in case (A) (left panel) brings thin sea-ice and associated melting further offshore. The section shown in figure S3, at 32°W, is roughly normal to pack ice south of Greenland and shows the relative ice-ocean meridional velocity; a series of energetic near-inertial waves events lead to a more extensive MIZ in case (A), while ice pack expansion in (B) is suppressed due to its retention of thicker ice. Additional CIOD iterations appear to better synchronize the ice within an incrementally updated approach. Figure S4 compares results with (A) and (C) $\Delta_T \Delta_t^{-1} = 2$, which lies between (A) and (B) which has the maximum number of CIOD iterations. Additional reconciliation of the ice thickness distribution (eqn B5) between CIOD iterations appears to provide improved representation of the MIZ. Further evaluation is warranted and will likely require tuning to the ice thermal energy balance in order to compensate for changes introduced by reductions in bottom melt rates.

Figure S5 shows SIV in both hemispheres in A01 ($\Delta_T \Delta_t^{-1} = 4$)and A02 ($\Delta_T \Delta_t^{-1} = 1$). Summer SIV increases in both hemispheres with additional CIOD iterations. In figure S6, Winter SIE is slightly higher in A02, with a more pronounced decrease in Summer. A01 appears more consistent with observations in the Arctic but is degraded in the Southern hemisphere with thicker and more persistent ice compared to satellite-based estimates.

Author contributions.

M.H wrote the initial model draft of the manuscript, with figure and text contributions from Y.J. for section 4.1. T.C. collaborated on use of the previously untested interspersed ocean/ice coupling and implemented fixes in early versions of the code. R.H. wrote intial code submissions in support of MOM6/SIS2 coupling. A.A. advised in the original implementation of the freshwater closure and model configuration. H.K. collaborated on initial model configuration development. W.C. and C.M. contributed to workflow and diagnostic development. U.W. ran and managed the simulation and post-processing. All authors contributed revisions.

Competing interests. The authors of this study have no competing interests.

https://doi.org/10.5194/egusphere-2026-6374
Preprint. Discussion started: 20 November 2026
© Author(s) 2026. CC BY 4.0 License.



Acknowledgements. We acknowledge the MOM6/SIS2/FMS development community for making this study possible and the ocean observational community for motivating model-data comparisons. Alan Wallcraft, for help porting the HYCOM grid and bathymetry to MOM6. Mitch Bushuk, Kate Hedstrom and Dmitry Dukhovskoy for discussions regarding SIS2 rheology and thermodynamics. Special thanks to Tony Rosati for his continued support and insight, Mitch Bushuk and Joseph Mouallem for providing valuable internal reviews, and Ritu Harrison for editing assistance. Analysis was done using Python with Xarray and Matplotlib, along with the broader ecosystem of openly available Python packages.

https://doi.org/10.5194/egusphere-2026-6374
Preprint. Discussion started: 20 November 2026
© Author(s) 2026. CC BY 4.0 License.

References

Adcroft, A., Hallberg, R., and Harrison, M.: A finite volume discretization of the pressure gradient force using analytic integration, Ocean Modelling, 22, 106–113, 2008.

Adcroft, A., Anderson, W., Balaji, V., Blanton, C., Bushuk, M., Dufour, C. O., Dunne, J. P., Griffies, S. M., Hallberg, R. W., Harrison, M. J., Held, I., Jansen, M. F., John, J., Krasting, J. P., Langenhorst, A., Legg, S., Liang, Z., McHugh, C., Radhakrishnan, A., Reichl, B. G., Rosati, T., Samuels, B. L., Shao, A., Stouffer, R., Winton, M., Wittenberg, A. T., Xiang, B., Zadeh, N., and Zhang, R.: The GFDL Global Ocean and Sea Ice Model OM4.0: Model Description and Simulation Features, Journal of Advances in Modeling Earth Systems, p. 2019MS001726, https://doi.org/10.1029/2019MS001726, 2019.

Biló, T., Straneo, F., Holte, J., and Le Bras, I.-A.: Arrival of new great salinity anomaly weakens convection in the Irminger Sea, Geophysical Research Letters, 49, e2022GL098 857, 2022.

Bodner, A. S., Fox-Kemper, B., Johnson, L., Roekel, L. P. V., McWilliams, J. C., Sullivan, P. P., Hall, P. S., and Dong, J.: Modifying the Mixed Layer Eddy Parameterization to Include Frontogenesis Arrest by Boundary Layer Turbulence, Journal of Physical Oceanography, 53, 323–339, https://doi.org/10.1175/JPO-D-21-0297.1, 2023.

Caton Harrison, T., Biri, S., Bracegirdle, T. J., King, J. C., Kent, E. C., Vignon, É., and Turner, J.: Reanalysis representation of low-level winds in the Antarctic near-coastal region, Weather and Climate Dynamics, 3, 1415–1437, 2022.

Cavalieri, D. J., Parkinson, C. L., Gloersen, P., and Zwally, H. J.: Sea Ice Concentrations from Nimbus-7 SMMR and DMSP SSM/I-SSMIS Passive Microwave Data, Version 1, https://doi.org/10.5067/8GQ8LZQVL0VL, 1996.

Chassignet, E. P. and Xu, X.: On the Importance of High-Resolution in Large-Scale Ocean Models, Advances in Atmospheric Sciences, 38, 1621–1634, https://doi.org/10.1007/s00376-021-0385-7, 2021.

Chassignet, E. P., Hurlburt, H. E., Metzger, E. J., Smedstad, O. M., Cummings, J. A., Halliwell, G. R., Bleck, R., Baraille, R., Wallcraft, A. J., Lozano, C., et al.: US GODAE: global ocean prediction with the HYbrid Coordinate Ocean Model (HYCOM), Oceanography, 22, 64–75, 2009.

Chen, H. W., Alley, R. B., and Zhang, F.: Interannual Arctic sea ice variability and associated winter weather patterns: A regional perspective for 1979–2014, Journal of Geophysical Research: Atmospheres, 121, 14–433, 2016.

Cheng, L., Abraham, J., Goni, G., Boyer, T., Wijffels, S., Cowley, R., Gouretski, V., Reseghetti, F., Kizu, S., Dong, S., et al.: XBT science: Assessment of instrumental biases and errors, Bulletin of the American Meteorological Society, 97, 924–933, 2016.

Cohen, J., Zhang, X., Francis, J., Jung, T., Kwok, R., Overland, J., Ballinger, T., Bhatt, U., Chen, H., Coumou, D., et al.: Divergent consensuses on Arctic amplification influence on midlatitude severe winter weather, Nature Climate Change, 10, 20–29, 2020.

Delworth, T. L., Cooke, W. F., Adcroft, A., Bushuk, M., Chen, J.-H., Dunne, K. A., Ginoux, P., Gudgel, R., Hallberg, R. W., Harris, L., et al.: SPEAR: The next generation GFDL modeling system for seasonal to multidecadal prediction and projection, Journal of Advances in Modeling Earth Systems, 12, e2019MS001 895, 2020.

Dumont, D.: Marginal ice zone dynamics: history, definitions and research perspectives, Philosophical Transactions of the Royal Society A: Mathematical, Physical and Engineering Sciences, 380, 2022.

Feltham, D. L.: Sea ice rheology, Annu. Rev. Fluid Mech., 40, 91–112, 2008.

Ganachaud, A. and Wunsch, C.: Large-scale ocean heat and freshwater transports during the World Ocean Circulation Experiment, Journal of Climate, 16, 696–705, 2003.

https://doi.org/10.5194/egusphere-2026-6374
Preprint. Discussion started: 20 November 2026
© Author(s) 2026. CC BY 4.0 License.

Gnanadesikan, A. and Hallberg, R. W.: On the relationship of the Circumpolar Current to Southern Hemisphere winds in coarse-resolution ocean models, Journal of Physical Oceanography, 30, 2013–2034, 2000.

Godfrey, J.: The effect of the Indonesian Throughflow on the ocean circulation and heat exchange with the atmosphere, Journal of Geophysical Research: Oceans, 1996.

Golledge, N. R., Keller, E. D., Gossart, A., Malyarenko, A., Bahamondes-Dominguez, A., Krapp, M., Jendersie, S., Lowry, D. P., Alevropoulos-Borrill, A., and Notz, D.: Antarctic coastal polynyas in the global climate system, Nature Reviews Earth & Environment, 6, 126–139, 2025.

Gordon, A. L., Sprintall, J., Van Aken, H. M., Susanto, D., Wijffels, S., Molcard, R., Ffield, A., Pranowo, W., and Wirasantosa, S.: The Indonesian throughflow during 2004–2006 as observed by the INSTANT program, Dynamics of Atmospheres and Oceans, 50, 115–128, 2010.

Gregg, M. C., Sanford, T. B., and Winkel, D. P.: Reduced mixing from the breaking of internal waves in equatorial waters, Nature, 422, 513–515, 2003.

Griffies, S. M., Pacanowski, R. C., and Hallberg, R. W.: Spurious Diapycnal Mixing Associated with Advection in a Z-Coordinate Ocean Model, Monthly Weather Review, 128, 538–564, https://doi.org/10.1175/1520-0493(2000)128<0538:SDMAWA>2.0.CO;2, 2000.

Hallberg, R.: Using a Resolution Function to Regulate Parameterizations of Oceanic Mesoscale Eddy Effects, Ocean Modelling, 72, 92–103, https://doi.org/10.1016/j.ocemod.2013.08.007, 2013.

Hallberg, R.: Numerical Instabilities of the Ice/Ocean Coupled System, Clivar Exchanges. No. 65, 19 No. 2, 38–41, 2014.

Hallberg, R. and Adcroft, A.: Reconciling Estimates of the Free Surface Height in Lagrangian Vertical Coordinate Ocean Models with Mode-Split Time Stepping, Ocean Modelling, 29, 15–26, https://doi.org/10.1016/j.ocemod.2009.02.008, 2009.

Hallberg, R. and Gnanadesikan, A.: The role of eddies in determining the structure and response of the wind-driven Southern Hemisphere overturning: Results from the Modeling Eddies in the Southern Ocean (MESO) project, Journal of Physical Oceanography, 36, 2232–2252, 2006.

Harrison, M.: Source code repository for GLBC0p08_OM4, https://doi.org/10.5281/zenodo.6342239, 2026a.

Harrison, M.: GLBc0p08_OM4_jra_A01 model results, https://doi.org/10.5281/zenodo.23542230, 2026b.

Harrison, M. and Hallberg, R.: Pacific subtropical cell response to reduced equatorial dissipation, Journal of Physical Oceanography, 38, 1894–1912, 2008.

Harrison, M., Adcroft, A., Hallberg, R., and Sergienko, O.: Improved surface mass balance closure in ocean hindcast simulations, Journal of Advances in Modeling Earth Systems, 14, e2021MS002 888, 2022.

Held, I., Guo, H., Adcroft, A., Dunne, J., Horowitz, L., Krasting, J., Shevliakova, E., Winton, M., Zhao, M., Bushuk, M., et al.: Structure and performance of GFDL's CM4. 0 climate model, Journal of Advances in Modeling Earth Systems, 11, 3691–3727, 2019.

Henyey, F. S., Wright, J., and Flatté, S. M.: Energy and action flow through the internal wave field: An eikonal approach, Journal of Geophysical Research: Oceans, 91, 8487–8495, 1986.

Huang, B., Liu, C., Banzon, V., Freeman, E., Graham, G., Hankins, B., Smith, T., and Zhang, H.-M.: Improvements of the Daily Optimum Interpolation Sea Surface Temperature (DOISST) Version 2.1, Journal of Climate, 34, 2923 – 2939, https://doi.org/10.1175/JCLI-D-20-0166.1, 2021.

Hunke, E., Lipscomb, W., Jones, P., Turner, A., Jeffery, N., and Elliott, S.: CICE, the Los Alamos sea ice model, US Department of Energy (DOE) Software, p. 54, 2017.

https://doi.org/10.5194/egusphere-2026-6374
Preprint. Discussion started: 20 November 2026
© Author(s) 2026. CC BY 4.0 License.

Hunke, E. C. and Dukowicz, J. K.: An elastic–viscous–plastic model for sea ice dynamics, Journal of physical oceanography, 27, 1849–1867, 1997.

Ilıcak, M., Adcroft, A. J., Griffies, S. M., and Hallberg, R. W.: Spurious dianeutral mixing and the role of momentum closure, Ocean Modelling, 45, 37–58, 2012.

Jackson, L., Hallberg, R., and Legg, S.: A Parameterization of Shear-Driven Turbulence for Ocean Climate Models, Journal of Physical Oceanography, 38, 1033–1053, https://doi.org/10.1175/2007JPO3779.1, 2008.

Johns, W. E., Baringer, M. O., Beal, L., Cunningham, S., Kanzow, T., Bryden, H. L., Hirschi, J., Marotzke, J., Meinen, C., Shaw, B., et al.: Continuous, array-based estimates of Atlantic Ocean heat transport at 26.5 N, Journal of Climate, 24, 2429–2449, 2011.

Johns, W. E., Elipot, S., Smeed, D. A., Moat, B., King, B., Volkov, D. L., and Smith, R. H.: Towards two decades of Atlantic Ocean mass and heat transports at 26.5° N, Philosophical Transactions of the Royal Society A: Mathematical, Physical and Engineering Sciences, 381, 20220 188, https://doi.org/10.1098/rsta.2022.0188, 2023.

Johnson, G. C. and Purkey, S. G.: Refined estimates of global ocean deep and abyssal decadal warming trends, Geophysical Research Letters, 51, e2024GL111 229, 2024.

Käse, R. H., Girton, J. B., and Sanford, T. B.: Structure and variability of the Denmark Strait Overflow: Model and observations, Journal of Geophysical Research: Oceans, 108, 2003.

Kimmritz, M., Danilov, S., and Losch, M.: On the convergence of the modified elastic–viscous–plastic method for solving the sea ice momentum equation, Journal of Computational Physics, 296, 90–100, 2015.

Kusahara, K., Hasumi, H., and Tamura, T.: Modeling sea ice production and dense shelf water formation in coastal polynyas around East Antarctica, Journal of Geophysical Research: Oceans, 115, 2010.

Legg, S., Hallberg, R. W., and Girton, J. B.: Comparison of Entrainment in Overflows Simulated by Z-Coordinate, Isopycnal and Non-Hydrostatic Models, Ocean Modelling, 11, 69–97, https://doi.org/10.1016/j.ocemod.2004.11.006, 2006.

Levitus, S., Antonov, J. I., Boyer, T. P., Baranova, O. K., Garcia, H. E., Locarnini, R. A., Mishonov, A. V., Reagan, J. R., Seidov, D., Yarosh, E. S., et al.: World ocean heat content and thermosteric sea level change (0–2000 m), 1955–2010, Geophysical Research Letters, 39, 2012.

Malmberg, S.-A. and Jónsson, S.: Timing of deep convection in the Greenland and Iceland Seas, ICES Journal of Marine Science, 54, 300–309, https://doi.org/10.1006/jmsc.1997.0221, 1997.

Martin, T. and Adcroft, A.: Parameterizing the fresh-water flux from land ice to ocean with interactive icebergs in a coupled climate model, Ocean Modelling, 34, 111–124, 2010.

Meredith, M. P., Woodworth, P. L., Chereskin, T. K., Marshall, D. P., Allison, L. C., Bigg, G. R., Donohue, K., Heywood, K. J., Hughes, C. W., Hibbert, A., Hogg, A. M., Johnson, H. L., Jullion, L., King, B. A., Leach, H., Lenn, Y.-D., Morales Maqueda, M. A., Munday, D. R., Naveira Garabato, A. C., Provost, C., Sallée, J.-B., and Sprintall, J.: SUSTAINED MONITORING OF THE SOUTHERN OCEAN AT DRAKE PASSAGE: PAST ACHIEVEMENTS AND FUTURE PRIORITIES, Reviews of Geophysics, 49, https://doi.org/https://doi.org/10.1029/2010RG000348, 2011.

Moat, B. I., Smeed, D., Rayner, D., Johns, W. E., Smith, R. H., Volkov, D. L., Elipot, S., Petit, T., Kajtar, J. B., Baringer, M. O., et al.: Atlantic meridional overturning circulation observed by the RAPID-MOCHA-WBTS (RAPID-Meridional Overturning Circulation and Heatflux Array-Western Boundary Time Series) array at 26N from 2004 to 2024 (v2024. 1a)., 2026.

New, A. and Smythe-Wright, D.: Aspects of the circulation in the Rockall Trough, Continental Shelf Research, 21, 777–810, 2001.

Oka, A., Hasumi, H., Okada, N., Sakamoto, T. T., and Suzuki, T.: Deep convection seesaw controlled by freshwater transport through the Denmark Strait, Ocean Modelling, 15, 157–176, 2006.

https://doi.org/10.5194/egusphere-2026-6374
Preprint. Discussion started: 20 November 2026
© Author(s) 2026. CC BY 4.0 License.

Østerhus, S., Sherwin, T., Quadfasel, D., and Hansen, B.: The overflow transport east of Iceland, in: Arctic–Subarctic Ocean Fluxes: Defining the Role of the Northern Seas in Climate, pp. 427–441, Springer, 2008.

Portela, E., Rintoul, S. R., Herraiz-Borreguero, L., Roquet, F., Bestley, S., Van Wijk, E., Tamura, T., McMahon, C. R., Guinet, C., Harcourt, R., et al.: Controls on dense shelf water formation in four East Antarctic polynyas, Journal of Geophysical Research: Oceans, 127, e2022JC018 804, 2022.

Reichl, B. G. and Hallberg, R.: A Simplified Energetics Based Planetary Boundary Layer (ePBL) Approach for Ocean Climate Simulations., Ocean Modelling, 132, 112–129, https://doi.org/10.1016/j.ocemod.2018.10.004, 2018.

Reichl, B. G., Wittenberg, A. T., Griffies, S. M., and Adcroft, A.: Improving equatorial upper ocean vertical mixing in the noaa/gfdl om4 model, Earth and Space Science, 11, e2023EA003 485, 2024.

Riser, S. C., Freeland, H. J., Roemmich, D., Wijffels, S., Troisi, A., Belbéoch, M., Gilbert, D., Xu, J., Pouliquen, S., Thresher, A., et al.: Fifteen years of ocean observations with the global Argo array, Nature Climate Change, 6, 145–153, 2016.

Roullet, G. and Madec, G.: Salt conservation, free surface, and varying levels: a new formulation for ocean general circulation models, Journal of Geophysical Research: Oceans, 105, 23 927–23 942, 2000.

Sadourny, R.: The dynamics of finite-difference models of the shallow-water equations, Journal of Atmospheric Sciences, 32, 680–689, 1975.

Shao, A. E., Adcroft, A., Hallberg, R., and Griffies, S. M.: A general-coordinate, nonlocal neutral diffusion operator, Journal of Advances in Modeling Earth Systems, 12, e2019MS001 992, 2020.

Swingedouw, D., Mignot, J., Labetoulle, S., Guilyardi, E., and Madec, G.: Initialisation and predictability of the AMOC over the last 50 years in a climate model, Climate Dynamics, 40, 2381–2399, 2013.

Talley, L. D.: Closure of the global overturning circulation through the Indian, Pacific, and Southern Oceans: Schematics and transports, Oceanography, 26, 80–97, 2013.

Thorndike, A. S., Rothrock, D. A., Maykut, G. A., and Colony, R.: The thickness distribution of sea ice, Journal of Geophysical Research, 80, 4501–4513, 1975.

Tsujino, Hiroyuki, e. a.: JRA55 based dataset for driving ocean-sea-ice models (JRA55-do), https://doi.org/10.1016/j.ocemod.2018.07.002, 2018.

Tsujino, H., Urakawa, L. S., Griffies, S. M., Danabasoglu, G., Adcroft, A. J., Amaral, A. E., Arsouze, T., Bentsen, M., Bernardello, R., Böning, C. W., et al.: Evaluation of global ocean–sea-ice model simulations based on the experimental protocols of the Ocean Model Intercomparison Project phase 2 (OMIP-2), Geoscientific Model Development, 13, 3643–3708, 2020.

Tulloch, R. and Marshall, J.: Exploring Mechanisms of Variability and Predictability of Atlantic Meridional Overturning Circulation in Two Coupled Climate Models, Journal of Climate, 25, 4067 – 4080, https://doi.org/10.1175/JCLI-D-11-00460.1, 2012.

van Aken, H. M., Brodjonegoro, I. S., and Jaya, I.: The deep-water motion through the Lifamatola Passage and its contribution to the Indonesian throughflow, Deep Sea Research Part I: Oceanographic Research Papers, 56, 1203–1216, https://doi.org/https://doi.org/10.1016/j.dsr.2009.02.001, 2009.

Wang, J., Min, C., Ricker, R., Shi, Q., Han, B., Hendricks, S., Wu, R., and Yang, Q.: A comparison between Envisat and ICESat sea ice thickness in the Southern Ocean, The Cryosphere, 16, 4473–4490, https://doi.org/10.5194/tc-16-4473-2022, 2022.

Williams, G., Bindoff, N., Marsland, S., and Rintoul, S.: Formation and export of dense shelf water from the Adélie Depression, East Antarctica, Journal of Geophysical Research: Oceans, 113, 2008.

Winton, M.: A reformulated three-layer sea ice model, Journal of atmospheric and oceanic technology, 17, 525–531, 2000.

https://doi.org/10.5194/egusphere-2026-6374
Preprint. Discussion started: 20 November 2026
© Author(s) 2026. CC BY 4.0 License.



Winton, M., Hallberg, R., and Gnanadesikan, A.: Simulation of density-driven frictional downslope flow in z-coordinate ocean models, Journal of Physical Oceanography, 28, 2163–2174, 1998.

Zanna, L., Khatiwala, S., Gregory, J. M., Ison, J., and Heimbach, P.: Global reconstruction of historical ocean heat storage and transport, Proceedings of the National Academy of Sciences, 116, 1126–1131, 2019.

595 Zhang, J. and Rothrock, D.: A thickness and enthalpy distribution sea-ice model, Journal of Physical Oceanography, 31, 2986–3001, 2001.

Zhang, J. and Rothrock, D. A.: Modeling global sea ice with a thickness and enthalpy distribution model in generalized curvilinear coordinates, Monthly Weather Review, 131, 845–861, 2003.